

Boise State University

ScholarWorks

Materials Science and Engineering Faculty
Publications and Presentations

Micron School for Materials Science and
Engineering

11-2020

High-Performance Flexible Bismuth Telluride Thin Film from Solution Processed Colloidal Nanoplates

Madhusudan Kongara
Boise State University

Tony Varghese
Boise State University

Karthik Chinnathambi
Boise State University

Jesse Schimpf
Boise State University

Josh Eixenberger
Boise State University

See next page for additional authors

Publication Information

Hollar, Courtney; Lin, Zhaoyang; Kongara, Madhusudan; Varghese, Tony; Chinnathambi, Karthik; Schimpf, Jesse; . . . and Estrada, David. (2020). "High-Performance Flexible Bismuth Telluride Thin Film from Solution Processed Colloidal Nanoplates". *Advanced Materials Technologies*, 5(11), 1-8. <https://doi.org/10.1002/admt.202000600>

For a complete list of authors, please see the article.

Authors

Madhusudan Kongara, Tony Varghese, Karthik Chinnathambi, Jesse Schimpf, Josh Eixenberger, Paul H. Davis, Yaqiao Wu, and David Estrada

High-Performance Flexible Bismuth Telluride Thin Film from Solution Processed Colloidal Nanoplates

Courtney Hollar, Zhaoyang Lin, Madhusudan Kongara, Tony Varghese, Chinnathambi Karthik, Jesse Schimpf, Josh Eixenberger, Paul H. Davis, Yaqiao Wu, Xiangfeng Duan, Yanliang Zhang, and David Estrada*

Thermoelectric generators are an environmentally friendly and reliable solid-state energy conversion technology. Flexible and low-cost thermoelectric generators are especially suited to power flexible electronics and sensors using body heat or other ambient heat sources. Bismuth telluride (Bi_2Te_3) based thermoelectric materials exhibit their best performance near room temperature making them an ideal candidate to power wearable electronics and sensors using body heat. In this report, Bi_2Te_3 thin films are deposited on a flexible polyimide substrate using low-cost and scalable manufacturing methods. The synthesized Bi_2Te_3 nanocrystals have a thickness of 35 ± 15 nm and a lateral dimension of 692 ± 186 nm. Thin films fabricated from these nanocrystals exhibit a peak power factor of $0.35 \text{ mW m}^{-1}\text{K}^{-2}$ at 433 K, which is among the highest reported values for flexible thermoelectric films. In order to evaluate the flexibility of the thin films, static and dynamic bending tests are performed while monitoring the change in electrical resistivity. After 1000 bending cycles over a 50 mm radius of curvature, the change in electrical resistance of the film is 23%. Using Bi_2Te_3 solutions, the ability to print thermoelectric thin films with an aerosol jet printer is demonstrated, highlighting the potential of additive manufacturing techniques for fabricating flexible thermoelectric generators.

year 2022.^[2] A particularly interesting application is utilizing wearable biomedical devices to monitor physiological signals and transmit data wirelessly, such as electrocardiograms, blood pressure, heart rate, and oxygen saturation,^[3–5] all of which currently require external power sources for efficient operation. Traditional power sources used for wearable biomedical devices are lithium ion batteries which have an energy density of $2.88 \times 10^9 \text{ J m}^{-3}$.^[6] Limitations to rigid lithium batteries include the need to frequently recharge and/or replace them, as well as design constraints which can impact comfort associated with a wearable device. To overcome some of these challenges, recent progress in the design of flexible lithium ion batteries include the use of carbon nanotubes, graphene, carbon cloth, and conductive paper as electrode materials.^[7] Alternative power sources for flexible electronics include electromagnetic and electrostatic sources. Both electromagnetic and electrostatic power sources

1. Introduction

The explosive market growth for self-powered wearable electronics has amplified attention on thermoelectric generators (TEGs).^[1] In a Markets and Markets report, it is estimated that the wearable electronic market will reach \$51.6 billion by the

convert mechanical vibrations to electrical energy.^[8–11] A power density of $307 \text{ } \mu\text{W m}^{-3}$ has been reported for electromagnetic sources,^[12] while $5.8 \times 10^7 \text{ } \mu\text{W m}^{-3}$ can be produced for electrostatic sources.^[13] However, continual mechanical vibrations are required to create a steady source of energy, thus when the user stops moving, the power source is no longer functioning.


Dr. C. Hollar, Dr. D. Estrada
Department of Mechanical Engineering
University of Idaho
Boise, ID 83702, USA
E-mail: daveestrada@boisestate.edu

Dr. Z. Lin, Dr. X. Duan
Department of Chemistry and Biochemistry
University of California
Los Angeles, CA 90095, USA

Dr. M. Kongara, Dr. T. Varghese, Dr. C. Karthik, J. Schimpf,
Dr. J. Eixenberger, Dr. P. H. Davis, Dr. Y. Wu, Dr. D. Estrada
Micron School of Materials Science and Engineering
Boise State University
Boise, ID 83725, USA

Dr. J. Eixenberger, Dr. Y. Wu, Dr. D. Estrada
Center for Advanced Energy Studies
Micron School of Materials Science and Engineering
Boise State University
Boise, ID 83725, USA

Dr. Y. Zhang
Department of Aerospace and Mechanical Engineering
University of Notre Dame
Notre Dame, IN 46556, USA

 The ORCID identification number(s) for the author(s) of this article can be found under <https://doi.org/10.1002/admt.202000600>.

© 2020 The Authors. Published by Wiley-VCH GmbH. This is an open access article under the terms of the Creative Commons Attribution License, which permits use, distribution and reproduction in any medium, provided the original work is properly cited.

DOI: 10.1002/admt.202000600

TEGs have received considerable attention as an alternative power source due to the solid-state conversion between heat and electricity. As a result, TEGs can be powered independently of movement, making them ideal for power generation during limited mobility applications. TEGs can also be manufactured as an independent power source for flexible electronics or in combination with flexible lithium-ion batteries in order to prolong the battery life. Recent studies report that body heat powered TEGs can produce power in the 14.4 μW to 11.4 mW range^[14,15] with up to 500–700 μW increases attributed to an increase in physical activity.^[16–18] Also, flexible TEGs can be applied to irregular surfaces and conform to skin in order to take advantage of the highest temperature gradient within the human body.^[15] Therefore, TEGs could provide an ideal power source to address the fast growing market for wearable devices.^[1,19]

The efficiency of TEGs depends on a dimensionless property known as the figure of merit $ZT = S^2\sigma T/k$, where S , σ , k , and T are the Seebeck coefficient, electrical conductivity, thermal conductivity, and absolute temperature, respectively.^[20,21] The portion of the numerator, $S^2\sigma$, is referred to as the power factor. In order to obtain a high efficiency thermoelectric (TE) material, the Seebeck coefficient and electrical conductivity should be maximized while minimizing the thermal conductivity. Recently, nanostructured TE materials have exhibited superior ZT as compared to their bulk counterparts.^[22,23] The mean free path of electrons is typically smaller than that of phonons, allowing particle size and grain boundary scattering to be used as a mechanism to engineer the σ/k ratio in ZT .^[24,25] Despite significant ZT improvement in nanostructured TE materials, the expensive preparation and fabrication of high-performance TE materials limits their large-scale commercialization.^[22,23,26] While extensive studies have focused on traditional rigid bulk materials, flexible TE materials that are cost effective need to be developed in order to keep up with the growing demand for flexible electronics and sensors.^[1,15,27]

Bi_2Te_3 -based alloys are reported to have the best TE performance near room temperature.^[28] As a result, flexible TE Bi_2Te_3 devices make them an ideal candidate to power wearable electronics and sensors utilizing body heat. Physical vapor deposition methods, including sputtering,^[29,30] evaporation,^[31,32] and electrodeposition^[33–35] are common methods to fabricate flexible TE films. An alternative approach to flexible film fabrication involves wet chemistry methods such as microwave-assisted flash combustion^[36–38] and solution reaction.^[39,40] Although the physical vapor deposition approach has increased in popularity, the fabrication process is time consuming and expensive. Therefore, wet chemical methods are being explored as an alternative synthesis technique that is potentially both low-cost and commercially scalable. Previous work has shown that microwave-assisted wet chemical techniques can be used to create Bi_2Te_3 nanocrystals for high performance rigid TEGs.^[37,38] A power factor of 0.45 $\text{mW m}^{-1}\cdot\text{K}^{-2}$ was demonstrated for bulk Bi_2Te_3 based TEGs fabricated using the microwave-assisted wet chemical technique.^[36] However, utilizing a solution reaction wet chemical technique, power factor values between 1.2 and 1.9 $\text{mW m}^{-1}\cdot\text{K}^{-2}$ were achieved for bulk Bi_2Te_3 .^[39,40] Although bulk Bi_2Te_3 pellets using the solution reaction wet chemical technique results in a higher power factor than the microwave-assisted technique, this doesn't translate into thin film performance. Current solution

reaction thin films have reported relatively modest power factors of $0.686 \times 10^{-3} \text{ mW m}^{-1}\cdot\text{K}^{-2}$ underscoring the need for improved fabrication methods for thin films.^[41]

Here, we report a high-performance flexible Bi_2Te_3 thin film prepared from a colloidal nanoplate ink, synthesized using a scalable wet chemical technique. We produce Bi_2Te_3 nanoplates using salt precursors in an ethylene glycol (EG) solvent and polyvinylpyrrolidone (PVP) as the capping agent, which provides considerable solubility in various solvents^[42,43] for further solution based processing and ink development. The obtained nanoplates were dispersed in isopropyl alcohol (IPA) to form an easy-to-handle solution which could be subsequently used as the ink for wet deposition techniques, such as spin coating or aerosol jet printing (AJP). Flexible Bi_2Te_3 thin films were constructed by spin coating the ink solution on a polyimide substrate, followed by thermal annealing. The peak power factor of our spin-coated flexible film was 0.35 $\text{mW m}^{-1}\cdot\text{K}^{-2}$ at 433 K, an impressive three orders of magnitude greater than previous solution reaction based thin films and approaching values reported for bulk based TEGs.^[41] We also demonstrate the compatibility of our ink with AJP, an additive manufacturing technique adopted by the aerospace^[44,45] and electronics industries.^[46,47]

2. Results and Discussion

We have previously demonstrated that PVP and EG do not form a compact layer on the Bi_2Te_3 nanoplate, producing a relatively solvent free surface and a relatively low electron transfer inhibition from the capping agent that eventually leads to improved electrical properties.^[48] After growth of the nanoplates in an EG solution using PVP as the surfactant and capping agent (Figure 1a), the nanoplates were dispersed in IPA to form an easy-to-handle and stable ink solution, which can be used to spin coat or print thin films on various substrates such as flexible polyimide. The thickness of the final thin film could be easily tuned by adjusting the ink concentration and deposition conditions.

The smooth surface of the thin film is achieved due to the compaction of small nanoplates during the spin coating process as shown in the photograph and scanning electron microscopic (SEM) image in Figures 1b,c, respectively. The film shows excellent continuity due to the nanoplate's geometry of a large lateral width and small thickness. The combination of the large aspect ratio and spin coating process to create the thin films results in the close compaction of nanoplates during the spin coating process.^[48] From atomic force microscopy (AFM) measurements, the average thickness and width of the individual nanoplates is 35 ± 15 and 692 ± 186 nm, respectively. An AFM image of a representative flake is shown in Figure 1d with corresponding height (thickness) and width measurements indicated. Figures 1e,f present histograms of the nanoplate height and width distributions, respectively. Interestingly, our process results in nanoplates as thin as ≈ 6 nm, indicating a potential route towards 2D Bi_2Te_3 synthesis. Individual nanoplates exhibit different morphologies, including a pristine flat morphology, a screw-dislocation in the center of the flake as indicated by a triangular growth region, and a coarse morphology with rough edges and pores (Figure S1, Supporting Information).

Layered Bi_2Te_3 has a rhombohedral crystal structure in the space group of $D_{3d}^5\text{-R}(-3)\text{m}$ with a large unit cell (≈ 3 nm along

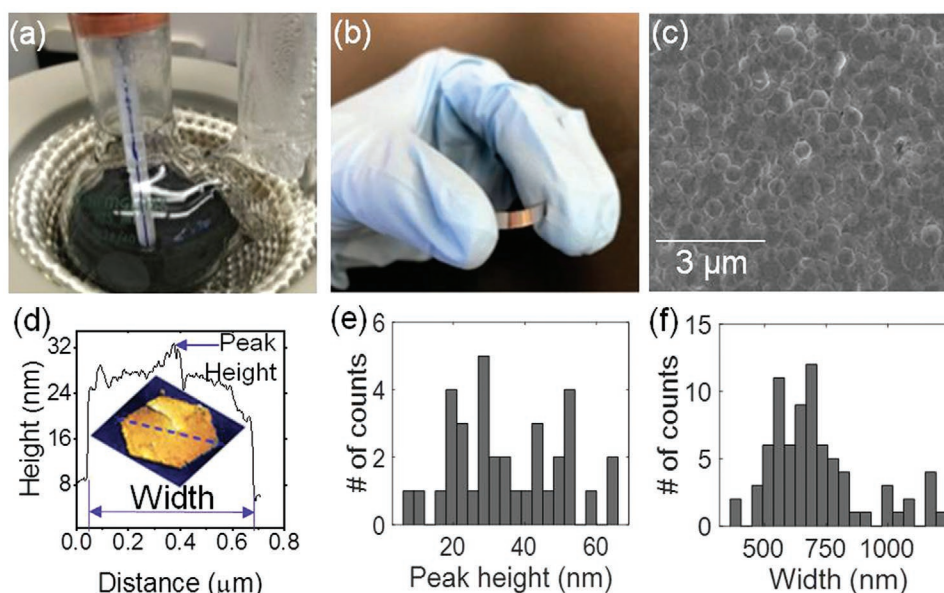


Figure 1. a) Optical image of wet chemical ink synthesis, b) optical image of spin coated Bi_2Te_3 thin film on polyimide substrate, c) SEM image of compaction of Bi_2Te_3 nanoplates resulting from the spin coating process, d) height versus distance plot of a representative Bi_2Te_3 nanoplate and AFM image of corresponding hexagonal nanoplate with blue dotted line indicating the cross-section measured across, e) histogram of nanoplate peak height distribution, f) histogram of nanoplate width distribution.

c axis) consisting of 15 layers of atoms, which are divided into three quintuple layers.^[49,50] Transmission electron microscopy (TEM) was used to study the size, morphology, and crystal structure of our Bi_2Te_3 nanoplates. **Figure 2a,b** shows the hexagonal shape of these nanoplates with edge to edge dimensions ranging from a few hundred nanometers to the micrometer scale, in good agreement with our AFM data. **Figure 2c** is a high-resolution lattice image from the same individual nanoplate as shown in **Figure 2b** and the corresponding [0001] zone-axis selected area diffraction pattern (**Figure 2c** inset). Electron diffraction studies indicate that these nanoplates are single crystalline and grow preferentially along the (0001) basal planes. The orientation of the bounding edges of the nanoplate obtained from the diffraction pattern is indicated with arrows in **Figure 2b**. The lattice image shown in **Figure 2c** further confirms the highly single crystalline nature of these nanoplates. The compositional homogeneity of these nanoplates was confirmed with energy-dispersive X-ray spectroscopy (EDS) line scans (**Figures S2 and S3**, Supporting Information). **Figure 2d,e** shows the energy filtered TEM (EFTEM) mapping of Bi-M and Te-M. This depicts the uniform distribution of these elements without any preferential segregation which is further validated by the EDS line scan performed from the center of a nanoplate to the edge as shown in **Figure 2f**. The large spikes in the Bi profile are attributed to noise during the measurement.

The in-plane Seebeck coefficient and electrical conductivity of spin-coated Bi_2Te_3 thin films were measured at elevated temperatures using a commercial Linseis Seebeck and resistivity instrument. Various samples with annealing temperatures ranging from 573 to 673 K were characterized in order to determine the optimal annealing temperature, the films maintain the same Bi_2Te_3 composition after annealing (**Figure S4**, Supporting Information). The maximum annealing temperature was

limited by the melting temperature of the substrate. All samples were measured from room temperature up to 483 K in order to prevent additional annealing and undesired structural changes (**Figure S5**, Supporting Information). The Seebeck coefficient first increases and then decreases with temperature, reaching a peak value at approximately 410 K. However, the electrical conductivity continues to increase with temperature, resulting in a maximum value at 483 K. **Figure 3a** demonstrates that as the annealing temperature increases, the room-temperature electrical conductivity increases from 1.8×10^4 to $2.9 \times 10^4 \text{ S m}^{-1}$. The higher annealing temperature is beneficial for removing any residual PVP on the surface and enhancing the interaction between nanoplates resulting in a higher electrical conductivity for the thin film.^[48,51] **Figure 3b** shows the Seebeck coefficient first increases and then decreases with annealing temperature, and the thin film annealed at 623 K exhibits the highest Seebeck coefficient. The power factor curve shown in **Figure 3c** demonstrates an increasing trend as the temperature increases until at least 433 K due to the temperature dependence of the electrical conductivity and Seebeck coefficient. A peak power factor of $0.35 \text{ mW m}^{-1} \cdot \text{K}^{-2}$ at 433 K is obtained in the film with an optimal annealing temperature of 623 K, indicating that the TE properties can be optimized by controlling the annealing temperature. In comparison, the peak power factor of $1.9 \text{ mW m}^{-1} \cdot \text{K}^{-2}$ for a nanostructured bulk Bi_2Te_3 pellet occurs at 375 K^[40] while a room temperature power factor of $0.686 \times 10^{-3} \text{ mW m}^{-1} \cdot \text{K}^{-2}$ is exhibited for a Bi_2Te_3 thin film annealed at 523 K.^[41]

In addition to creating thin films through spin coating, it is also possible to use AJP for thin film deposition of our colloidal inks. **Figure 4a** shows a schematic of the AJP process. During this process, the same Bi_2Te_3 ink used for spin coating films is aerosolized and printed on a polyimide substrate (**Figure 4b**). **Figures 4c,d** compare the cross-sectional scanning transmission

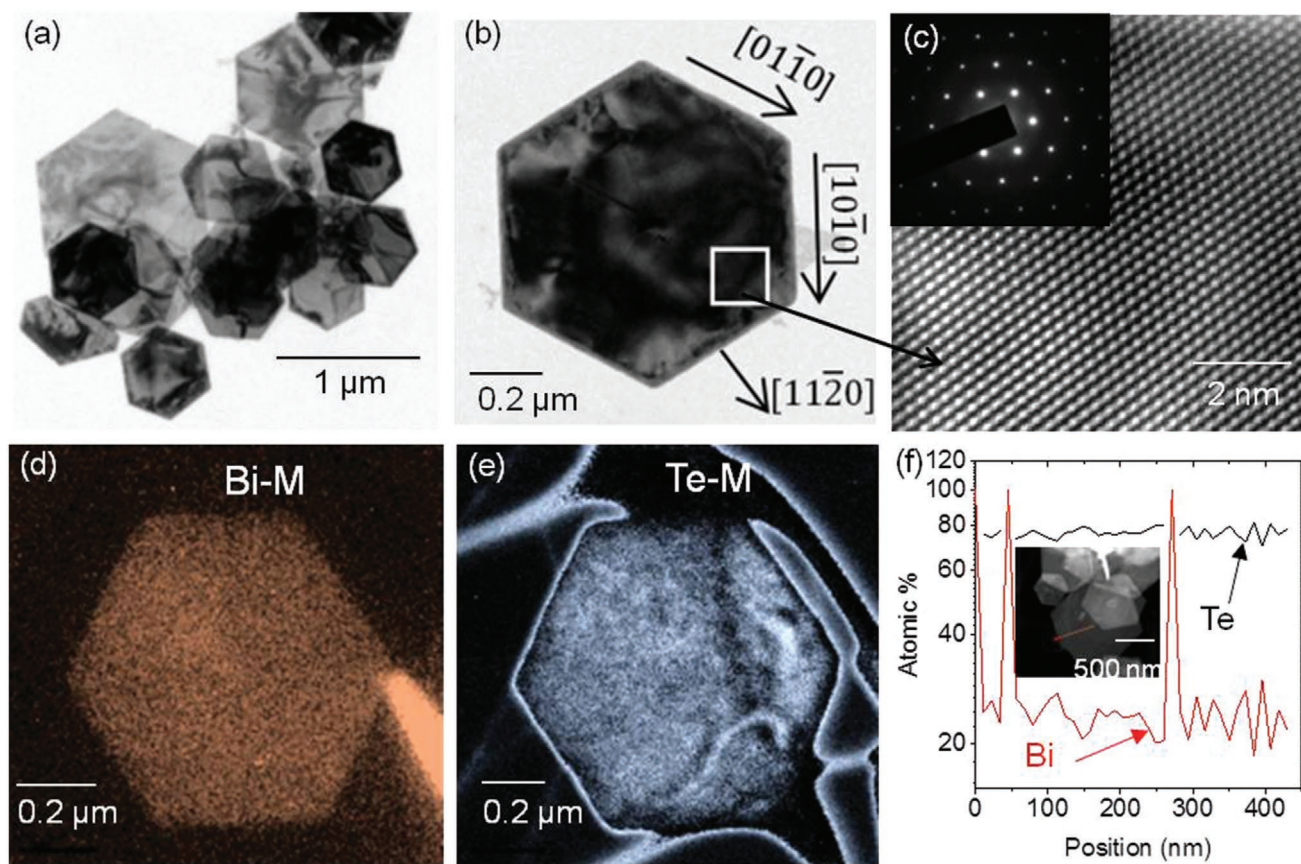


Figure 2. a) Low magnification bright-field TEM micrograph of the Bi_2Te_3 nanoplates showing their hexagonal shape, b) bright-field TEM image of an individual nanoplate with crystallographic orientation of the edges marked, c) a high-resolution lattice image recorded from the nanoplate shown in (b) and the inset shows the [0001] zone axis selected area electron diffraction pattern obtained from the same nanoplate, (d) and (e) show the EDS mapping of Bi-M and Te-M, respectively, indicating their uniform distribution, f) shows a EDS line scan of Bi and Te performed from the center of a nanoplate (inset) to the edge.

electron microscope (STEM) of spin coated and AJP films, respectively (see Figure S6, Supporting Information, for additional images). Spin coated films show a more layered nature to the flakes as compared to the more porous surface of AJP films. Furthermore, Figures 4e,f show the flake orientation for spin coated and AJP films, respectively. Due to the high aspect ratio

of lateral dimensions to thickness of the nanoplates, spin coated thin films form well stacked nanoplates. This creates a large contact area which results in a reduced interface resistance and less porous film. However, similar to graphene films, AJP results in an increase in porosity due to the random stacking of nanoplates as they adhere to the polyimide substrate,^[52] as well as

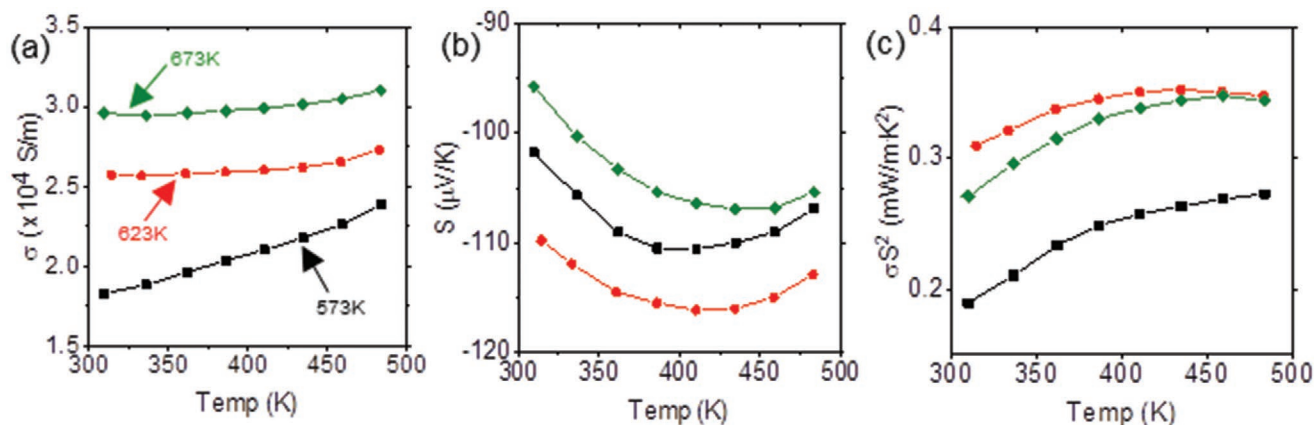


Figure 3. Thermoelectric performance of solution processed Bi_2Te_3 films spin coated onto a flexible polyimide substrate and annealed at various temperatures. a) Electrical conductivity σ , b) Seebeck coefficient S , and c) power factor σS^2 .

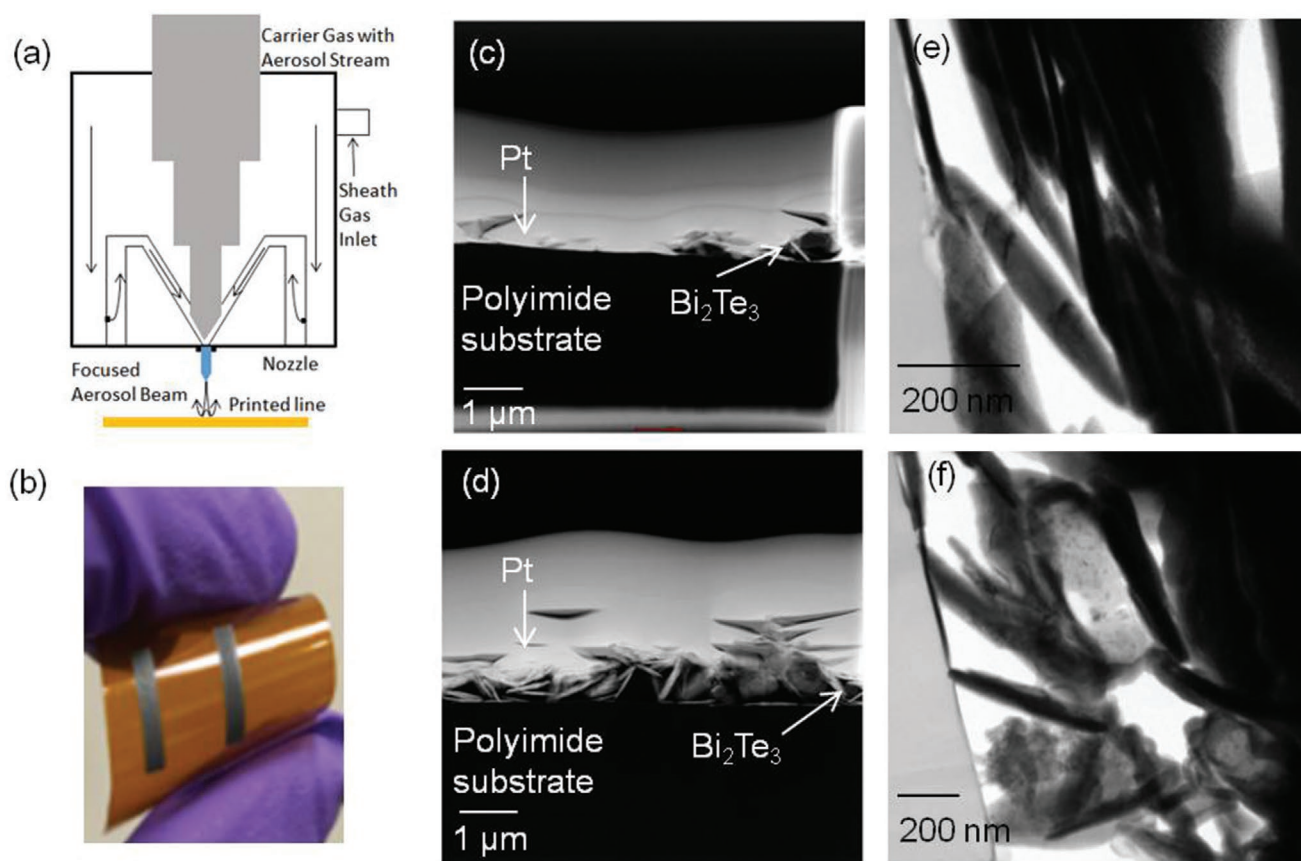


Figure 4. a) Schematic of the AJP process and b) a photograph of a 2 mm × 10 mm AJP Bi₂Te₃ flexible films on polyimide substrate. c) Cross-sectional STEM of spin coated Bi₂Te₃ film, d) cross-sectional STEM of AJP Bi₂Te₃ film, e) cross-sectional TEM of spin coated Bi₂Te₃ film showing flake orientation, and f) cross-sectional TEM of AJP Bi₂Te₃ film showing flake orientation.

potentially trapping solvents within the printed features. The solvents evaporate leaving behind pores, thus resulting in a larger electrical resistivity. The electrical conductivity of an aerosol jet printed Bi₂Te₃ film was 939.64 S m⁻¹. Meanwhile, the Seebeck coefficient was -64 μV K⁻¹. The decrease in electrical conductivity of aerosol jet printed films can be attributed to the increase in porosity,^[52] which also impacts the Seebeck coefficient. Due to the random arrangements of nanoplates and high amount of porosity, this hinders the interaction between the nanoparticles which results in a lower electrical conductivity and poor Seebeck voltage. In order to further enhance the TE properties of the aerosol jet printed films, an improvement in the ink particle concentration and a compaction method is necessary to reduce contact resistance and porosity. However, one 2 mm × 10 mm AJP film produced 0.238 mV using a Peltier device to mimic changes in human body temperature (Figure 5a), demonstrating the feasibility of this approach with further optimization.

The spin coated and AJP films were further evaluated for flexibility by performing room-temperature electrical resistance measurements using the van der Pauw method. The electrical resistance was selected as the property to evaluate flexibility since cracking of the film can greatly affect the electrical resistance. Static bend tests were performed on five different radii of curvature (ROC): 10, 20, 30, 40, and 50 mm. Bending spin coated Bi₂Te₃ thin films around a 10 mm ROC resulted in the highest

change in resistance of 17%, while the 50 mm ROC showed the lowest change in resistance of 5% (Figure 5b, inset). A dynamic bend test was then performed over a 50 mm ROC (Figure 5b). After 100 cycles, the electrical resistance of the film showed less than a 13% increase and a 23% increase after 1000 cycles. By comparison, sputtered indium tin oxide (ITO) thin films, a common transparent conductor used in diverse optoelectronic devices, exhibited an increase in resistance of 518% after 1000 bending cycles for a 10 mm ROC.^[48] Additionally, the Bi₂Te₃ films fabricated using alternative additive manufacturing techniques were tested after dynamic bending. For comparison, the aerosol jet printed Bi₂Te₃ showed an increased resistance of 7% after 1000 bending cycles over a 50 mm ROC and our previously reported screen-printed films had an increase in resistance of 4.5% for 150 bend cycles over a 5 mm ROC.^[53] The smaller increase in resistance for screen-printed and aerosol jet printed Bi₂Te₃ films, when compared to the spin coated films, can be attributed to a higher film thickness. As a result, the film is more robust and is less sensitive to electrical resistance changes during bending tests.

3. Conclusion

In conclusion, we have reported on high-performance flexible Bi₂Te₃ thin films fabricated from a facile ink solution obtained

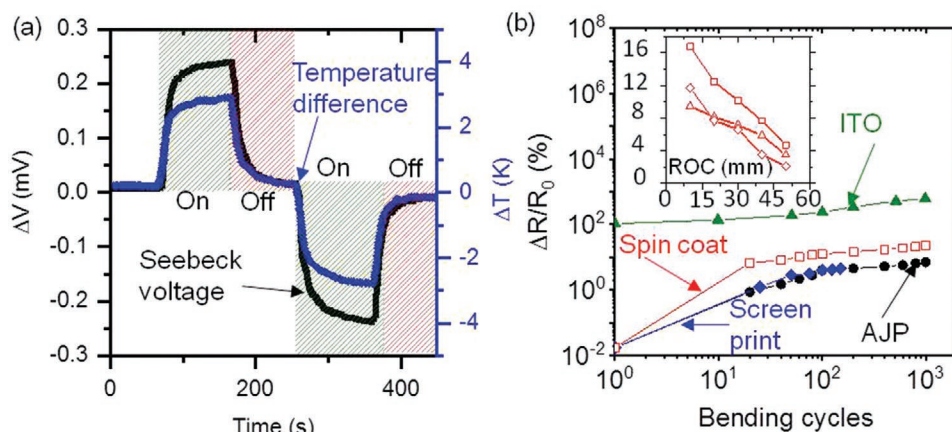


Figure 5. a) Voltage produced by a one leg AJP device using a Peltier device to mimic changes in body temperature. b) Resistance changes of flexible films as a function of bending cycles for spin coated Bi_2Te_3 for a 50 mm ROC as compared to sputtered ITO for a 10 mm ROC, screen printed Bi_2Te_3 for a 5 mm ROC, and AJP Bi_2Te_3 literature values for a 50 mm ROC. Inset graph is the resistance change of several flexible films as a function of various bending radii.

using a low-cost and scalable solution reaction process. The ink solution is formulated by the Bi_2Te_3 nanoplates dispersion in proper solvent, which exhibits a great potential for the practical large-scale production compared with the conventional CVD approaches or high-temperature flux methods. Bi_2Te_3 thin films annealed at 623 K exhibit a power factor of $0.35 \text{ mW m}^{-1} \text{ K}^{-2}$ at 433 K which is comparable to values obtained for bulk samples. The samples exhibited a 23% increase in electrical resistance over a 50 mm radius of curvature after 1000 bending cycles, showing flexibility for our spin coated samples. The low-cost and scalable fabrication process of Bi_2Te_3 films demonstrates the potential to power flexible electronics, sensors, and medical devices as compared to their bulk counterparts.

4. Experimental Section

Chemicals: Bismuth nitrate pentahydrate ($\text{Bi}(\text{NO}_3)_3 \cdot 5\text{H}_2\text{O}$, >99.9%), sodium tellurite (NaTeO_3 , >99.5%), sodium hydroxide (NaOH , >99%), poly(vinyl pyrrolidone) (PVP, MW $\approx 40\,000$), and EG were all purchased from Sigma-Aldrich. All the chemicals were used as received without further purification.

Solution-Phase Synthesis of Bi_2Te_3 Nanoplatelets: 0.2 mmol $\text{Bi}(\text{NO}_3)_3 \cdot 5\text{H}_2\text{O}$ (0.0970 g), 0.3 mmol NaTeO_3 (0.0665 g), 4 mmol NaOH (0.1600 g), and 2 mmol PVP (0.2223 g) were mixed with 10 mL ethylene glycol. The mixture was stirred for ≈ 10 min to fully dissolve all solids and then heated to 190 °C (in about 12 min) in a 25 mL three-neck flask equipped with a thermocouple and reflux condenser in a heating mantle. After 3 h, the heating mantle was removed and the mixture was allowed to cool down to room temperature naturally. The mixture was then centrifuged at 10 000 rpm for 10 min after the addition of 20 mL isopropanol and 10 mL acetone. The supernatant was discarded and the solid was dispersed in another 40 mL isopropanol assisted by sonication. The washing steps were repeated with isopropanol two more times to remove the excessive ethylene glycol, PVP, and other impurities. The final product was dispersed in isopropanol in various concentrations for further characterization.

Spin Coat Deposition of Bi_2Te_3 Film on Plastic Substrates: The dispersion of Bi_2Te_3 in isopropanol was centrifuged at 3000–4000 rpm for 3 min. The upper dispersion (the top half) was carefully taken out with pipette and the bottom precipitated solid was discarded. This step removes the aggregated nanocrystals, which is critical to obtain the high-quality thin film. The dispersion was spin coated onto an oxygen-plasma-treated polyimide substrate (90 W, 3 min) at a speed of 1000–2000 rpm. Multiple spin coating

processes were repeated in order to achieve thicker films. For the post deposition thermal treatment, the films were typically annealed on a hot plate inside of an argon-filled glove box at 300–400 °C (573 K–673 K) for 1 h.

Aerosol Jet Printing of Bi_2Te_3 Film on Plastic Substrates: TE thin films were printed with an Optomec Aerosol Jet 200 system using the UA-max atomizer. A recirculating bath temperature of 20 °C helped to stabilize the ink temperature and prevented the output from being too solvent rich. A tool platen temperature of 40 °C was used to ensure drying of the ink once on the substrate, and to minimize oxidation of TE powders while exposed to open air. TE ink exhibited good atomization at 0.450 mA, and the nitrogen flow for the sheath and atomizer were set to 80 and 35 sccm, respectively. TE material was deposited on a polyimide substrate with a 200 μm inner diameter ceramic nozzle and polyethylene tubing. While printing, the nozzle was kept at a constant distance of 3 mm from the substrate, and a serpentine filling pattern having a 30–40% overlap was utilized for the 2 mm by 10 mm printed structures. Printed samples were further dried in an inert glove box, and sintered under argon atmosphere at 350 °C for 1 h.

AFM Characterization: Bi_2Te_3 nanoplates were imaged using a Bruker Dimension Icon AFM housed in an inert argon environment containing <0.1 ppm H_2O and O_2 . Imaging was performed using a ScanAsyst-Air probe (Bruker, 2 nm nominal radius of curvature) operating in PeakForce Tapping mode. Once acquired, the images were processed with a first order flatten to remove sample tip and tilt as well as any line-to-line offsets in the Z-axis. Thirty-five nanoplates were imaged to derive statistics. The height of each nanoplate was recorded as the peak value from the substrate, excluding any particulates present in the image. Width measurements were obtained for each of the three pairs of sides on the hexagonal nanoplates and averaged to report a lateral dimension.

SEM Characterization: SEM characterizations were performed using scanning electron microscopy (SEM, JEOL JSM-6700F FE-SEM) with an acceleration voltage of 5 kV.

TEM Ink Characterization: TEM samples were prepared by diluting the ink with isopropyl alcohol and drop casting onto a 300 mesh TEM Cu grid coated with a carbon support film. Bright-field, high resolution lattice imaging and selected area electron diffraction studies were carried out using a JEOL 2100 HR TEM operated at 200 kV. EDS line scans and EELS/EFTEM were performed using a FEI Tecnai G² F30 STwin STEM operated at 300 kV.

TEM Film Characterization: The TEM lamellas were prepared using lift-out technique in a FEI Quanta 3D FEG dual-beam focused ion beam. Microstructure characterization was carried out by using a FEI Tecnai G² F30 STEM FEG STEM at 300 kV. Both bright-field imaging technique in TEM mode and Z-contrast imaging technique in STEM mode were utilized to reveal fine structures of the flakes and porosity of the two samples. EDS technique was used to confirm sample composition.

Thermoelectric Measurement: Temperature-dependent in-plane Seebeck coefficient and electrical conductivity measurements were performed simultaneously using a commercial Linseis Seebeck and Resistivity instrument in a helium atmosphere. Determining the Seebeck coefficient consisted of measuring the Seebeck voltage and the temperature difference established in parallel to the sample surface. The electrical resistivity measurements used a linear four-probe configuration. The measurement uncertainties are less than 3% for the Seebeck coefficient and 2% for the electrical conductivity.

Supporting Information

Supporting Information is available from the Wiley Online Library or from the author.

Acknowledgements

This project was supported by NASA award No. ID-80NSSC17M0029. C.H. was supported by the National Science Foundation Graduate Research Fellowship Program under Grant No. 1545659. The inert atmosphere Bruker Dimension Icon atomic force microscope system was funded by NSF MRI Award No. 1727026. The authors would like to acknowledge Katelyn Wada for help with ink synthesis, the Microscopy and Characterization Suite (MaCS), Center for Advanced Energy Studies (CAES) for help with cross-sectional TEM imaging, and Olivia Maryon of the Boise State Surface Science Lab for helpful discussions and assistance with AFM imaging, analysis, and interpretation. X.D. acknowledged the support from the US Department of Energy, Office of Basic Energy Sciences, Division of Materials Science and Engineering through award DE-SC0018828. Y.Z. would like to acknowledge funding support from the National Science Foundation under award CMMI-1747685. D.E. acknowledges career development support from Institutional Development Awards (IDeA) from the National Institute of General Medical Sciences of the National Institutes of Health under Grants Nos. P20GM103408 and P20GM109095.

Conflict of Interest

The authors declare no conflict of interest.

Keywords

aerosol jet printing, bismuth telluride, flexible thermoelectrics

Received: June 19, 2020

Revised: August 18, 2020

Published online: October 9, 2020

- [1] J. H. Bahk, H. Y. Fang, K. Yazawa, A. Shakouri, *J. Mater. Chem. C* **2015**, 3, 10362.
- [2] "Wearable Technology Market." Market Research Firm, www.marketsandmarkets.com/Market-Reports/wearable-electronics-market-983.html (accessed: February 2020).
- [3] R. G. Haahr, S. Duun, E. V. Thomsen, K. Hoppe, J. Branebjerg, presented at 2008 5th Int. Summer School and Symp. on Medical Devices and Biosensors, Hong Kong, China June **2008**.
- [4] D. Son, J. Lee, S. Qiao, R. Ghaffari, J. Kim, J. E. Lee, C. Song, S. J. Kim, D. J. Lee, S. W. Jun, S. Yang, M. Park, J. Shin, K. Do, M. Lee, K. Kang, C. S. Hwang, N. S. Lu, T. Hyeon, D. H. Kim, *Nat. Nanotechnol.* **2014**, 9, 397.
- [5] M. G. Sun, J. D. Fernstrom, W. Y. Jia, S. A. Hackworth, N. Yao, Y. C. Li, C. L. Li, M. H. Fernstrom, R. J. Sclabassi, *J. Amer. Diet. Ass.* **2010**, 110, 45.
- [6] S. Roundy, D. Steingart, L. Frechette, P. Wright, J. Rabaey, in *Wireless Sensor Networks*, Springer, Berlin **2004**.
- [7] G. Zhou, F. Li, H.-M. Cheng, *Energy Environ. Sci.* **2014**, 7, 1307.
- [8] M. Rasouli, L. S. J. Phee, *Expert Rev. Med. Devices* **2010**, 7, 693.
- [9] C. B. Williams, C. Shearwood, M. A. Harradine, P. H. Mellor, T. S. Birch, R. B. Yates, *IEE Proc. Circ. Dev. Syst.* **2001**, 148, 337.
- [10] E. Romero, R. O. Warrington, M. R. Neuman, *Physiol. Meas.* **2009**, 30, R35.
- [11] S. Meninger, J. O. Mur-Miranda, R. Amirtharajah, A. P. Chandrakasan, J. H. Lang, *IEEE Trans. VLSI Syst.* **2001**, 9, 64.
- [12] S. P. Beeby, R. N. Torah, M. J. Tudor, P. Glynn-Jones, T. O'Donnell, C. R. Saha, S. Roy, *J. Micromech. Microeng.* **2007**, 17, 1257.
- [13] A. M. Paracha, P. Basset, F. Marty, A. Vaisman Chasin, P. Poulichet, T. Bourouina, arXiv:0802.3063, **2008**.
- [14] Y. Yang, X.-J. Wei, J. Liu, *J. Phys. D: Appl. Phys.* **2007**, 40, 5790.
- [15] S. J. Kim, J. H. We, B. J. Cho, *Energy Environ. Sci.* **2014**, 7, 1959.
- [16] M. A. Karami, D. J. Inman, *Appl. Phys. Lett.* **2012**, 100.
- [17] L. S. Y. Wong, S. Hossain, A. Ta, J. Edvinsson, D. H. Rivas, H. Naas, *IEEE J. Solid-State Circuits* **2004**, 39, 2446.
- [18] V. Leonov, in *Wearable Monitoring Systems*, Vol. 27, Springer US, Boston, MA **2011**.
- [19] J. D. MacKenzie, C. Ho, *Proc. IEEE* **2015**, 103, 535.
- [20] D. M. Rowe, *CRC Handbook of Thermoelectrics*, CRC Press, Boca Raton, FL **1995**.
- [21] H. J. Goldsmid, *Applications of Thermoelectric Refrigeration*, Springer, Boston, MA **1964**, pp. 210–223.
- [22] K. Biswas, J. He, I. D. Blum, C.-I. Wu, T. P. Hogan, D. N. Seidman, V. P. Dravid, M. G. Kanatzidis, *Nature* **2012**, 489, 414.
- [23] B. Poudel, Q. Hao, Y. Ma, Y. Lan, A. Minnich, B. Yu, X. Yan, D. Wang, A. Muto, D. Vashaee, *Science* **2008**, 320, 634.
- [24] A. Khitun, A. Balandin, J. L. Liu, K. L. Wang, *J. Appl. Phys.* **2000**, 88, 696.
- [25] M. Scheele, N. Oeschler, K. Meier, A. Kornowski, C. Klinke, H. Weller, *Adv. Funct. Mater.* **2009**, 19, 3476.
- [26] J.-F. Li, W.-S. Liu, L.-D. Zhao, M. Zhou, *NPG Asia Mater.* **2010**, 2, 152.
- [27] Z. Lu, M. Layani, X. Zhao, L. P. Tan, T. Sun, S. Fan, Q. Yan, S. Magdassi, H. H. Hng, *Small* **2014**, 10, 3551.
- [28] E. Ashalley, H. Chen, X. Tong, H. Li, Z. M. Wang, *Front. Mater. Sci.* **2015**, 9, 103.
- [29] K. Kusagaya, H. Hagino, S. Tanaka, K. Miyazaki, M. Takashiri, *J. Electron. Mater.* **2015**, 44, 1632.
- [30] J. X. Zhang, Q. Li, P. J. Niu, Q. X. Yang, B. M. Tan, X. H. Niu, B. H. Gao, *Mater. Res. Innovations* **2015**, 19, S10.
- [31] M. Takashiri, K. Kurita, H. Hagino, S. Tanaka, K. Miyazaki, *J. Appl. Phys.* **2015**, 118, 065301.
- [32] J.-M. Lin, Y.-C. Chen, C.-P. Lin, H.-C. Chien, C.-Y. Wen, J.-Y. Chang, Z.-Y. Zhan, *Microelectron. Eng.* **2015**, 148, 51.
- [33] K. Kato, Y. Hatasako, M. Kashiwagi, H. Hagino, C. Adachi, K. Miyazaki, *J. Electron. Mater.* **2014**, 43, 1733.
- [34] C. V. Manzano, B. Abad, M. M. Rojo, Y. R. Koh, S. L. Hodson, A. M. L. Martinez, X. Xu, A. Shakouri, T. D. Sands, T. Borca-Tasciuc, *Sci. Rep.* **2016**, 6, 19129.
- [35] M. Yamaguchi, H. Yamamuro, M. Takashiri, *Curr. Appl. Phys.* **2018**, 18, 1513.
- [36] H. Kaur, L. Sharma, S. Singh, B. Sivaiah, G. B. Reddy, T. D. Senguttuvan, *J. Electron. Mater.* **2014**, 43, 1782.
- [37] Y. Du, K. F. Cai, S. Chen, P. Cizek, T. Lin, *ACS Appl. Mater. Interfaces* **2014**, 6, 5735.
- [38] Z. Cao, E. Koukharenko, M. J. Tudor, R. N. Torah, S. P. Beeby, *Sens. Actuators, A* **2016**, 238, 196.
- [39] J. S. Son, M. K. Choi, M.-K. Han, K. Park, J.-Y. Kim, S. J. Lim, M. Oh, Y. Kuk, C. Park, S.-J. Kim, *Nano Lett.* **2012**, 12, 640.

- [40] M. Hong, Z.-G. Chen, L. Yang, J. Zou, *Nanoscale* **2016**, *8*, 8681.
- [41] T. Wang, R. Mehta, C. Karthik, P. G. Ganesan, B. Singh, W. Jiang, N. Ravishankar, T. Borca-Tasciuc, G. Ramanath, *J. Phys. Chem. C* **2010**, *114*, 1796.
- [42] Y. Zhang, L. P. Hu, T. J. Zhu, J. Xie, X. B. Zhao, *Cryst. Growth Des.* **2013**, *13*, 645.
- [43] M. M. Rashad, A. El-Dissouky, H. M. Soliman, A. M. Elseman, H. M. Refaat, A. Ebrahim, *Mater. Res. Innovations* **2018**, *22*, 315.
- [44] J. A. Paulsen, M. Renn, K. Christenson, R. Plourde, presented at *2012 Future of Instrumentation Int. Workshop (FIW) Proc.*, Gatlinburg, TN October **2012**.
- [45] A. K. Noor, *Structures Technology for Future Aerospace Systems*, American Institute of Aeronautics and Astronautics, Reston, VA **2000**.
- [46] J. M. Hoey, M. T. Reich, A. Halvorsen, D. Vaselaar, K. Braaten, M. Maassel, I. S. Akhatov, O. Ghandour, P. Drzaic, D. L. Schulz, *IEEE Trans. Adv. Packag.* **2009**, *32*, 809.
- [47] C. Goth, S. Putzo, J. Franke, presented at *2011 IEEE 61st Electronic Components and Technology Conf. (ECTC)*, Lake Buena Vista, FL May–June **2011**.
- [48] Z. Y. Lin, Y. Chen, A. D. Yin, Q. Y. He, X. Q. Huang, Y. X. Xu, Y. A. Liu, X. Zhong, Y. Huang, X. F. Duan, *Nano Lett.* **2014**, *14*, 6547.
- [49] D. Kong, W. Dang, J. J. Cha, H. Li, S. Meister, H. Peng, Z. Liu, Y. Cui, *Nano Lett.* **2010**, *10*, 2245.
- [50] G. Zhang, B. Kirk, L. A. Jauregui, H. Yang, X. Xu, Y. P. Chen, Y. Wu, *Nano Lett.* **2012**, *12*, 56.
- [51] Z. Lin, C. Hollar, J. S. Kang, A. Yin, Y. Wang, H. Y. Shiu, Y. Huang, Y. Hu, Y. Zhang, X. Duan, *Adv. Mater.* **2017**, *29*, 201606662.
- [52] T. Pandhi, E. Kreit, R. Aga, K. Fujimoto, M. T. Sharbati, S. Khademi, A. N. Chang, F. Xiong, J. Koehne, E. M. Heckman, D. Estrada, *Sci. Rep.* **2018**, *8*, 10842.
- [53] T. Varghese, C. Hollar, J. Richardson, N. Kempf, C. Han, P. Gamarachchi, D. Estrada, R. J. Mehta, Y. Zhang, *Sci. Rep.* **2016**, *6*, 33135.